

# Dynamics of thermal plumes in three-dimensional isoviscous thermal convection

Shijie Zhong

Department of Physics, University of Colorado at Boulder, Boulder, CO 80309, USA. E-mail: szhong@spice.colorado.edu

Accepted 2005 March 9. Received 2005 March 9; in original form 2004 August 31

## SUMMARY

The dynamics of mantle plumes are important for understanding intraplate volcanism and heat transfer in the mantle. Using 3-D numerical models and scaling analyses, we investigated the controls of convective vigour or  $Ra$  (Rayleigh number) on the dynamics of thermal plumes in isoviscous and basal heating thermal convection. We examined the  $Ra$  dependence of plume number, plume spacing, plume vertical velocity and plume radius. We found that plume number does not increase monotonically with  $Ra$ . At relatively small  $Ra$  ( $\leq 10^6$ ), plume number is insensitive to  $Ra$ . For  $3 \times 10^6 \leq Ra \leq 3 \times 10^7$ , plume number scales as  $Ra^{0.31}$  and plume spacing  $\lambda \sim Ra^{-0.16} \sim \delta^{1/2}$ , where  $\delta$  is the thickness of the thermal boundary layer. However, for larger  $Ra$  ( $\sim 10^8$ ) plume number and plume spacing again become insensitive to  $Ra$ . This indicates that the box depth poses a limit on plume spacing and plume number. We demonstrate from both scaling analyses and numerical experiments that the scaling exponents for plume number,  $n$ , heat flux,  $\beta$ , and average velocity on the bottom boundary,  $v$ , satisfy  $n = 4\beta - 2v$ . Our scaling analyses also suggest that vertical velocity in upwelling plumes  $V_{up} \sim Ra^{2(1-n+\beta/2)/3}$  and that plume radius  $R_{up} \sim Ra^{(\beta-1-n/2)/3}$ , which differ from the scalings for the bottom boundary velocity and boundary layer thickness.

**Key words:** mantle convection, mantle plumes.

## 1 INTRODUCTION

Information about the dynamics of mantle upwelling plumes is important for understanding the surface tectonics and dynamic evolution of the Earth. Mantle plumes may be the main sources for interplate volcanism (i.e. hotspots) (Wilson 1963; Morgan 1963) and large igneous provinces (Morgan 1981; Richards *et al.* 1989). They are also responsible for large-scale swell topography, including the Hawaiian swell (Sleep 1987; Davies 1988; Olson 1990). Because mantle plumes result from instabilities of a bottom thermal boundary layer (TBL) of the convective mantle (Morgan 1963), they are important agents in the release of heat to the shallow regions of the mantle from either the core, for a compositionally uniform mantle (i.e. whole mantle convection) (Davies 1988; Sleep 1990), or the bottom layer, for a layered mantle (Davies 1998), thus affecting the dynamic evolution of the Earth. A significant amount of effort has been made in the last 30 yr to improve our understanding of the dynamics of mantle plumes, particularly of the number of plumes and their heat transfer properties. Early estimates of hotspot numbers based on surface observations of hotspot volcanism range from 50 to 100 (Burke & Wilson 1976; Crough 1983). However, only some 30 hotspots display swell-topography and gravity anomalies (Crough 1983; Davies 1988; Sleep 1990). Improved seismic imaging techniques may help identify mantle plumes (Wolfe *et al.* 1997; Romanowicz & Gung 2002; Zhao 2004; Courtillot *et al.* 2003). A

more recent seismic study reports about 30 mantle plumes, most of which are related to surface hotspots (Montelli *et al.* 2004).

Transport of heat flux by mantle plumes can be constrained by the hotspot swell topography and gravity anomalies (Davies 1988; Sleep 1990). The estimated plume heat flux differs greatly (by a factor of  $\sim 20$ ) among different plumes with Hawaii as the largest, transferring  $\sim 1$  per cent of the heat at the Earth's surface. The total plume heat flux is estimated to be 3–5 TW, which is  $\sim 10$  per cent of the total heat flux from the Earth's mantle, and has been attributed to the cooling of the core (Davies 1988; Sleep 1990). Davies (1998) also used this relatively small plume heat flux as evidence for whole mantle convection that is driven mostly by internal heating. Davies (1998) argued that if the lower mantle were more enriched with radioactive elements, as in the conventional layered mantle model, plume heat flux would be significantly greater than 3–5 TW as constrained by the swell topography and gravity anomalies because significantly more heat from the bottom layer (i.e. the lower mantle) needs to be released via the plumes.

However, the actual heat flux via mantle plumes and its relation to the heat flux out of the core (or the bottom layer of a layered mantle) is controversial. Malamud & Turcotte (1999) suggested that the size distribution of mantle plumes follows a power law and that there might be as many as 5000 mantle plumes that transport 13 TW heat flux to the base of lithosphere to account for reduced topographic subsidence at areas of old seafloor. Malamud & Turcotte (1999)

further suggested that the majority of the plumes are too weak to produce any significant surface expression. If their proposal is true, this suggests that the estimated 3–5 TW plume heat flux from surface hotspots may not preclude layered convection. However, Malamud & Turcotte (1999) did not discuss physical mechanisms that may be responsible for such a distribution of mantle plumes. Another question is how much heat flux from the core is actually transported via mantle plumes? Part of the heat flux from the core may be consumed to heat up cold downwellings that reach the core–mantle boundary (Labrosse 2002) and this part of core heat flux is not included in the plume heat flux inferred from surface topography and geoid (Davies 1988; Sleep 1990) that only measures convective heat flux with respect to the upper mantle background temperature.

The dynamics of thermal plumes is the key to understanding the controls on plume numbers and plume heat transfer. The dynamics of thermal plumes has been investigated in the laboratory and in theoretical and numerical studies. In laboratory studies, Weeraratne & Manga (1998) showed that for thermal convection at large Rayleigh number  $Ra$  with rigid boundaries, thermal plumes replace large-scale structures and become the dominant features. Laboratory studies also demonstrated that upwelling plumes are influenced by downwelling plumes (Schaeffer & Manga 2001) and by plate motion (Jellinek *et al.* 2003; Gonnermann *et al.* 2004). Theoretical and numerical studies have been more directly aimed at the problem of plume number. A Rayleigh–Taylor instability analysis has been used to investigate the dependence of plume number and plume spacing  $\lambda$  on the thickness of an unstable layer  $\delta$  (e.g. the bottom thermal boundary layer) (e.g. Ribe & Devalpine 1994). However, the Rayleigh–Taylor analysis does not consider the thermal energy balance and temporal evolution of structure. Solomatov (2004) examined the dependence of aspect ratio of convection cells and plume spacing on convective vigour (i.e.  $Ra$ ) in 2-D stagnant lid convection. Because the 3-D geometry may be important for plume dynamics, 3-D Cartesian models of plume dynamics have been formulated for basal heating (Malevsky & Yuen 1993) or entirely volumetric heating (Parmentier *et al.* 1994) convection with uniform viscosity. The study by Parmentier & Sotin (2000) was the first to systematically examine the dependence of plume number on  $Ra$  for 3-D isoviscous convection with entirely volumetric heating.

In this paper we present 3-D Cartesian isoviscous convection models with basal heating and scaling analyses for the plume dynamics. We focus on the number, size (i.e. cross-sectional area), vertical velocity and heat transfer of thermal plumes and their  $Ra$  dependence. The paper is organized as follows: Section 2 presents the numerical methods and scaling analyses; we will then show results of plume dynamics from numerical models and compare them with the scaling analyses before presenting our discussion and conclusion.

## 2 NUMERICAL MODELS AND METHODS

### 2.1 Description of the models

We consider thermal convection with basal heating and constant viscosity in a 3-D Cartesian geometry. The governing equations are the conservation equations of mass, momentum and energy under the Boussinesq approximation (e.g. McKenzie *et al.* 1974). The equations are non-dimensionalized with temporal and spatial scales of  $D^2/\kappa$  and  $D$ , respectively, and a temperature scale of  $\Delta T$ , where

$D$  is the thickness of the box,  $\kappa$  is the thermal diffusivity and  $\Delta T$  is the temperature difference between the bottom and the top boundaries. The only controlling parameter in our models is the Rayleigh number  $Ra$  which is defined as

$$Ra = \frac{\rho g \alpha \Delta T D^3}{\eta \kappa}, \quad (1)$$

where  $\rho$ ,  $\eta$  and  $\alpha$  are respectively the density, viscosity and thermal expansion coefficient and  $g$  is the gravitational acceleration.

We consider models in boxes with different sizes:  $1 \times 1 \times 1$ ,  $2 \times 2 \times 1$  and  $3 \times 3 \times 1$  in 3-D. The surface and bottom boundaries are free-slip and isothermal with the non-dimensional temperatures fixed to be 0 and 1, respectively. Reflecting boundary conditions (i.e. thermally insulating and mechanically free-slip) are applied to all the vertical boundaries. The initial temperature for steady-state cases at relatively small  $Ra$  is the linear temperature profile superimposed by sinusoidal perturbations of a given wavelength with details that will be discussed later. The initial temperature for time-dependent cases at large  $Ra$  is the linear temperature profile superimposed by small random perturbations ( $10^{-3}$ ).

To solve the governing equations we use a finite-element code CITCOM (Moresi & Solomatov 1995) with significant enhancements including parallel computing (Zhong *et al.* 2000). We compute our models for a sufficiently large number of timesteps to either a steady state or a statistically steady state. We then analyse these steady-state results.

### 2.2 Quantifying model results

In addition to the standard outputs of the flow velocity, temperature and surface and bottom heat fluxes (i.e. the Nusselt number,  $Nu$ ), we also quantify the convective heat flux and dynamic properties of plumes. In the interior of convective flow, conductive heat flux can be ignored compared with convective heat flux. Non-dimensional convective heat flux at any location  $(x, y, z)$  is defined as

$$H_{\text{adv}} = u_z (T - T_{\text{ave}}(z)), \quad (2)$$

where  $T$  is the temperature,  $u_z$  is the vertical velocity and  $T_{\text{ave}}(z)$  is the horizontally averaged temperature at vertical position  $z$ . This definition of convective heat flux is consistent with that for plume heat flux that is dependent on plume excess temperature (e.g. Davies 1988; Sleep 1990). This convective heat flux can also be related to other geophysical observations, including seismic tomography, that often measure anomalies with respect to background values. However, it should be pointed out that convective heat flux can be defined without subtracting  $T_{\text{ave}}(z)$  in (2) to get the same net convective heat flux across a surface because of the mass conservation.

It is clear from eq. (2) that cold downwellings (i.e.  $u_z < 0$  and  $T < T_{\text{ave}}(z)$ ) produce positive (i.e. upward) convective heat flux, just like what hot upwellings (i.e.  $u_z > 0$  and  $T > T_{\text{ave}}(z)$ ) do. For the isoviscous and basal heating convection considered in this study cold downwellings and hot upwellings are each responsible for 50 per cent of heat flux at the surface and bottom boundaries; this is because  $|u_z|$  and  $|T - T_{\text{ave}}(z)|$  are the same for upwelling and downwelling plumes and also because the total convective heat flux is constant at any depth outside of the TBLs and is equal to heat flux at the surface and bottom boundaries.

To quantify the dynamic properties of plumes we first use the following procedures to identify downwelling and upwelling plumes:

(1) For a given depth  $z$ , go through all the elements to identify those for upwellings and downwellings with the following criteria.

An element is a upwelling element if

$$T > T_{\text{avg}}(z) + f(T_{\text{max}}(z) - T_{\text{ave}}(z)), \quad (3)$$

or is a downwelling element if

$$T < T_{\text{avg}}(z) + f(T_{\text{min}}(z) - T_{\text{ave}}(z)). \quad (4)$$

In eqs (3) and (4),  $T_{\text{max}}(z)$  and  $T_{\text{min}}(z)$  are the maximum and minimum temperature at vertical position  $z$ , and  $f$  is a constant that determines threshold temperatures for upwellings and downwellings. The smaller  $f$  is, the larger the area of upwellings and downwellings is at this depth. We used  $f$  ranging from 0.1 to 0.4, and the effects of  $f$  will be discussed later. This step is similar to that in Labrosse (2002).

(2) At this depth, go through all the upwelling (downwelling) elements and group them into individual upwelling (downwelling) plumes. For each plume, find its area, heat flux and vertical velocity. Find the total number of plumes  $N_p$  and of upwelling plumes  $N_{\text{up}}$ . In determining the number of plumes we only include plumes that carry no less than 5 per cent of the heat that is carried by the strongest plume (note that the plume heat flux for different hotspots may vary by a factor of 20; Sleep 1990). We call this threshold  $P_f$ . The effects of thresholds  $P_f$  on our analyses are also examined.

(3) Repeat steps (1) and (2) for a range of depths ( $0.45 \leq z \leq 0.55$ , i.e. the mid-depth section of the box) and find the averaged properties for plumes (i.e. plume radius, heat flux and vertical velocity).

For steady-state cases in addition to the algorithm outlined above we also determine the radius of an upwelling plume  $R_{\text{up}}$  by fitting plume temperature in the depth range of  $0.45 \leq z \leq 0.55$  to

$$T(r) = T_0 + \Delta T \exp[-(r/R_{\text{up}})^2], \quad (5)$$

where  $T(r)$  is the temperature as a function of the distance from the centre of the upwelling plume,  $T_0$  is the temperature at a large distance and parameters  $R_{\text{up}}$  and  $\Delta T$  are the fitting parameters. However, this algorithm is only feasible for steady-state cases. After  $R_{\text{up}}$  is obtained, we determine the area and average vertical velocity of plumes.

### 2.3 A scaling analysis for plume dynamics

An important question that we want to answer in this study is how plume number depends on the convective vigour or  $Ra$ . This question can also be rephrased as how the plume spacing depends on  $Ra$ . It is well known that  $Nu$  or heat flux increases with  $Ra$  to a power of  $\sim 1/3$  for basal heating and isoviscous convection. As  $Ra$  increases, does the number of plumes need to increase in order to enhance heat transfer? Or can the increased heat flux be accomplished with increased convective heat flux for each plume without increasing the number of plumes?

For thermal convection with high  $Ra$  Howard (1966) proposed that the thermal boundary layer (TBL) thickens conductively before becoming unstable when the TBL reaches a critical thickness (i.e. a local  $Ra$  reaches a critical value). When becoming unstable, TBLs produce upwelling or downwelling plumes.

Suppose that for thermal convection in 3-D, the number of plumes including downwelling and upwelling  $N_p \sim Ra^n$ , then the average spacing between downwelling and upwelling plumes  $\lambda \sim D(1/N_p)^{1/2} \sim DRa^{-n/2}$  (notice that for basal heating and isoviscous convection the average spacing between upwelling plumes is

$2\lambda$  and the number of upwelling plumes is  $\sim N_p/2$ ). Let us consider the bottom TBL that thickens with time starting from below a downwelling. The critical TBL thickness  $\delta \sim (\kappa t)^{1/2}$  where  $t = \lambda/u_b$  and  $u_b$  is an averaged horizontal velocity at the bottom boundary. Suppose that  $u_b \sim (\kappa/D)Ra^v$ , then we have  $\delta \sim (\kappa \lambda/u_b)^{1/2} \sim DRa^{-n/4-v/2}$ . Also because  $Nu \sim Ra^\beta$ ,  $\delta \sim DNu^{-1} \sim DRa^{-\beta}$ . Therefore, we have the following relationship between the scaling exponents  $n$ ,  $\beta$  and  $v$ :

$$n = 4\beta - 2v. \quad (6)$$

Since  $\beta$  is often found to be  $\sim 1/3$  for basal heating and isoviscous convection, this simple analysis indicates that the scaling for  $N_p$  or plume spacing  $\lambda$  depends critically on the scaling for velocity. For thermal convection in 2-D, a similar analysis leads to  $n = 2\beta - v$ . From a boundary layer theory (e.g. Turcotte & Schubert 2002) for 2-D convection,  $\beta = 1/3$  and  $v = 2/3$ , this implies that  $n = 0$ , i.e. the number of plumes is independent of  $Ra$ .

We can also derive scaling for plume radius  $R_{\text{up}}$  and plume vertical velocity  $V_{\text{up}}$  on  $Ra$ . For a cylindrical upwelling plume, if we ignore its vertical variations, the force balance between the plume's buoyancy force and viscous traction is

$$\pi R_{\text{up}}^2 \rho g \alpha \Delta T_{\text{up}} = 2\pi R_{\text{up}} \eta (dV/dr)_{r=R_{\text{up}}}, \quad (7)$$

where  $V$  and  $\Delta T_{\text{up}}$  are the vertical velocity and excess temperature of the plume and  $r$  is the distance from the centre of the plume. For basal heating and isoviscous convection we have  $\Delta T_{\text{up}} \sim \Delta T$ , and  $(dV/dr)_{r=R_{\text{up}}} \sim V_{\text{up}}/\lambda$ , where  $\Delta T$  is the temperature difference between the top and bottom boundaries and  $\lambda$  is the plume spacing. This leads to

$$V_{\text{up}} \sim \lambda R_{\text{up}} \rho g \alpha \Delta T / \eta, \quad (8)$$

or

$$V_{\text{up}} \sim \frac{\kappa}{D^3} \lambda R_{\text{up}} Ra \sim \frac{\kappa}{D^2} R_{\text{up}} Ra^{1-n/2}, \quad (9)$$

where in (9)  $\lambda \sim D(1/N_p)^{1/2} \sim DRa^{-n/2}$  was used.

The energy balance leads to

$$N_p \rho C \Delta T_{\text{up}} V_{\text{up}} \pi R_{\text{up}}^2 \sim k \frac{\Delta T}{D} Nu \sim k \frac{\Delta T}{D} Ra^\beta. \quad (10)$$

Substituting  $\Delta T_{\text{up}} \sim \Delta T$ ,  $N_p \sim Ra^n$  and (9) into (10) leads to the scaling of plume radius with  $Ra$ :

$$R_{\text{up}} \sim DRa^{(\beta-1-n/2)/3}. \quad (11)$$

Combining (11) and (9), we have the scaling of plume vertical velocity with  $Ra$ :

$$V_{\text{up}} \sim \frac{\kappa}{D} Ra^{2(1-n+\beta/2)/3}. \quad (12)$$

In particular, if  $n = 0$  (i.e. the number of plumes is independent of  $Ra$ ) and  $\beta = 1/3$ , (11) and (12) suggest that  $R_{\text{up}} \sim Ra^{-2/9}$  and  $V_{\text{up}} \sim Ra^{7/9}$ , differing from the scaling for the thickness of TBLs and velocity on the bottom boundary. For  $n > 0$ ,  $R_{\text{up}}$  decreases more rapidly with  $Ra$ , while  $V_{\text{up}}$  increases more slowly with  $Ra$ , compared with  $n = 0$ .

This analysis appears to be incomplete, as we do not explicitly give  $n$  which affects the scaling for  $R_{\text{up}}$  and  $V_{\text{up}}$ . However, as we will demonstrate with our numerical experiments, for basal heating and isoviscous convection there does not seem to be a simple and monotonic dependence of  $N_p$  or  $\lambda$  on  $Ra$ . However, eqs (6), (11) and (12) are satisfied over a wide range of model parameters that are considered in this study.

**Table 1.** Model parameters and  $Nu$  and  $u_b$ .

Case	$Ra$	Box size	Mesh size <sup>a</sup>	$Nu$	$u_b$
1	$10^4$	$1 \times 1 \times 1$	$48 \times 48 \times 48$	4.72	31.77
2	$3 \times 10^4$	$1 \times 1 \times 1$	$48 \times 48 \times 48$	7.32	72.5
3	$10^5$	$1 \times 1 \times 1$	$48 \times 48 \times 48$	11.24	165.4
4	$3 \times 10^5$	$1 \times 1 \times 1$	$48 \times 48 \times 48$	16.10	335.7
5	$10^6$	$1 \times 1 \times 1$	$64 \times 64 \times 64$	23.45	710.5
6	$3 \times 10^6$	$1 \times 1 \times 1$	$64 \times 64 \times 64$	29.28(1.51) <sup>b</sup>	1472(110)
7	$10^4$	$3 \times 3 \times 1$	$96 \times 96 \times 48$	5.12[4.54] <sup>c</sup>	49.8[63.7]
8	$3 \times 10^4$	$3 \times 3 \times 1$	$96 \times 96 \times 48$	7.44[6.21]	104.3[123.1]
9	$10^5$	$3 \times 3 \times 1$	$96 \times 96 \times 48$	10.8[8.82]	223.3[244]
10	$3 \times 10^5$	$3 \times 3 \times 1$	$96 \times 96 \times 48$	14.3[–]	397.9[–]
11	$3 \times 10^6$	$2 \times 2 \times 1$	$128 \times 128 \times 64$	27.1(1.0)	1642(153)
12	$10^7$	$2 \times 2 \times 1$	$192 \times 192 \times 96$	41.2(1.9)	3085(348)
13	$3 \times 10^7$	$2 \times 2 \times 1$	$256 \times 256 \times 96$	57.3(1.9)	5162(507)
14	$10^8$	$2 \times 2 \times 1$	$320 \times 320 \times 96$	82.1(2.4)	11012(1018)

<sup>a</sup>The mesh is refined in the vertical direction near the TBLs, depending on  $Ra$ .

<sup>b</sup>The numbers in round brackets for  $Nu$  and  $u_b$  are the standard deviations which are negligibly small for cases 1–5 and 7–10.

<sup>c</sup>The numbers in the square brackets for  $Nu$  and  $u_b$  are the steady-state values for cases 7–9, while those before the brackets are the quasi-steady-state values.

### 3 RESULTS

#### 3.1 Number and spacing of plumes

We computed 14 models with boxes of different sizes,  $Ra$  ranging from  $10^4$  to  $10^8$  and different initial conditions (Table 1). We first present a series of cases with relatively small  $Ra$  that reach a steady state, before showing intrinsically time-dependent cases at higher  $Ra$ . Cases 1–5 are in a  $1 \times 1 \times 1$  box with  $Ra$  ranging from  $10^4$  to  $10^6$  and initial conditions

$$T(x, z) = 1 - z + \delta T \sin(\pi z) \cos\left(\frac{\pi x}{L}\right) \cos\left(\frac{\pi y}{L}\right), \quad (13)$$

where  $\delta T = 10^{-3}$  and  $L = 1$ . For all these cases, grid refinement is applied to the bottom and top boundary layers according to  $Ra$ .

For these cases, a steady-state solution was achieved with two downwelling plumes at two diagonal corners of the box and two upwelling plumes at the other two corners (Figs 1a and b). Here our steady state is an absolute steady state in which the numerical solutions of heat flux and velocity do not vary with time (Fig. 2). When a higher  $Ra$  (e.g. case 6 with  $3 \times 10^6$ ) was used, the solution becomes time dependent and we do not obtain the simple flow structure (Fig. 1c) as in cases with small  $Ra$ . For each of these steady-state cases we computed steady-state solutions of average surface heat flux (i.e.  $Nu$ ) and average bottom velocity  $u_b$  (Table 1 and Fig. 2: note that Fig. 2 uses a transit time which is defined as the product of time and a characteristic velocity or the steady-state velocity  $u_b$ ). The steady-state values of  $Nu$  and  $u_b$  are fitted to power-law functions of  $Ra$ :  $Nu = 0.201Ra^{0.347}$  and  $u_b = 0.0683Ra^{0.673}$  (Figs 3a and b and Table 2). From eq. (6),  $\beta = 0.347$  and  $\nu = 0.673$  lead to

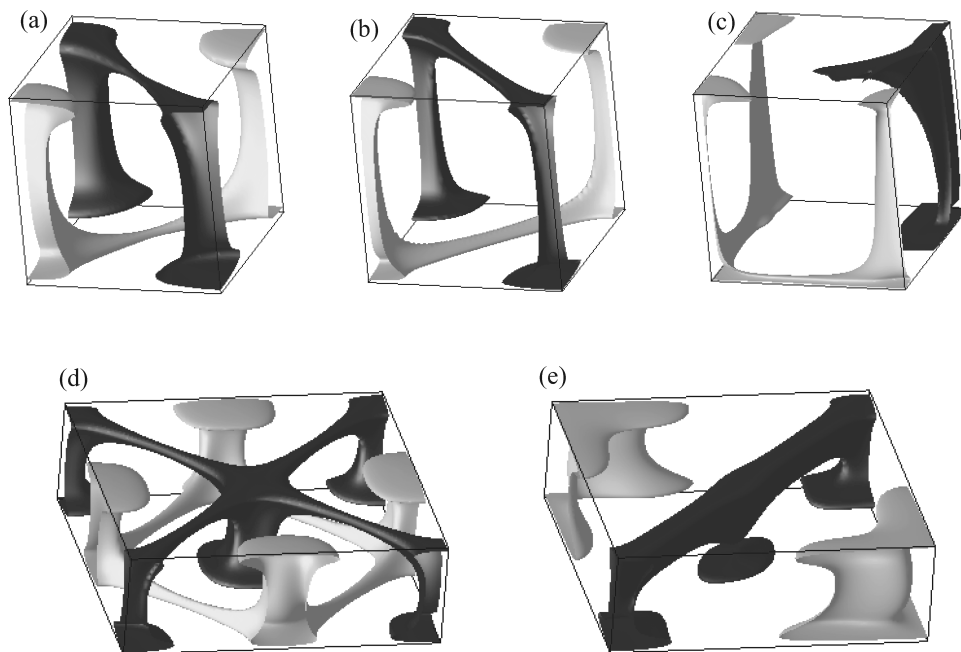


**Figure 1.** 3-D thermal structure for cases 2 (a), 4 (b), 6 (c) and 8 (d) and quasi-steady state and final steady state (e). The figure shows isosurfaces of residual temperature  $\delta T = T - T_{ave}(z)$  with  $\delta T = 0.2$  (light shading) and  $-0.2$  (dark shading), respectively.

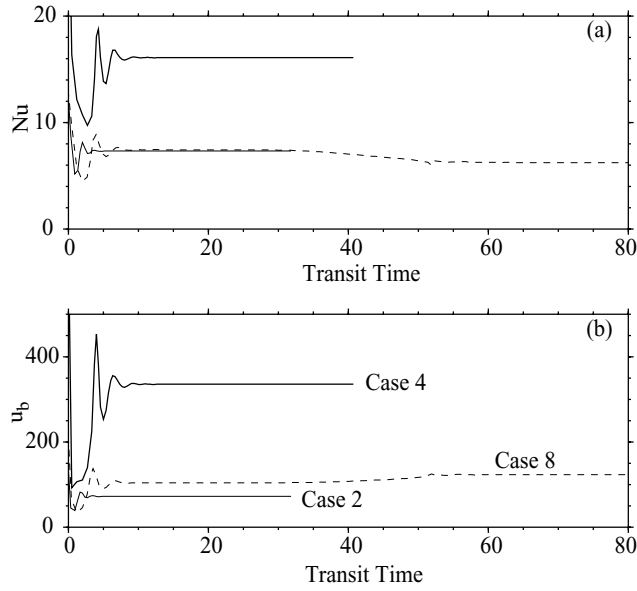


**Figure 2.** Time dependence of  $Nu$  (a) and  $u_b$  (b) for cases 2, 4 and 8. Notice that transit time is used here and that parts (a) and (b) use the same line convention.

$n = 0.04$ . The negligibly small  $n$  implies that the number of plumes  $N_p$  is independent of  $Ra$ , which is consistent with the results for cases 1–5.

We now present cases 7–10 with  $Ra$  ranging from  $10^4$  to  $3 \times 10^5$  in a  $3 \times 3 \times 1$  box (Table 1). For these four cases we use the same ini-

tial conditions as those for cases 1–6 but with  $L = 3/2$ . These cases first reach a quasi-steady state with nine equally spaced and alternating upwelling and downwelling plumes (Fig. 1d). The solutions are stable at this state for a period of time before changing into another state (Fig. 2). Cases 7–9 eventually reach and stay at a steady state in which only five plumes survive (Fig. 1e), while case 10 with  $Ra = 3 \times 10^5$  becomes time dependent. For these cases we compute  $Nu$  and  $u_b$  for the quasi-steady state and steady state (except for case 10 that does not reach a steady state) separately (Table 1) and fit them to the power-law functions of  $Ra$  (Table 2). For the quasi-steady-state solutions for these four cases  $Nu = 0.322Ra^{0.303}$  and  $u_b = 0.182Ra^{0.613}$ , and for the steady-state solutions for cases 7–9  $Nu = 0.326Ra^{0.286}$  and  $u_b = 0.298Ra^{0.583}$  (Table 2 and Fig. 3). According to eq. (6), these exponents for  $Nu$  and  $u_b$  suggest that  $n$  is  $-0.01$  and  $-0.02$  for the quasi-steady state and steady state, respectively, which is consistent with the modelling results that the number of plumes for these cases is the same at their respective states. It is interesting to notice that although  $Nu$ ,  $u_b$  and their scaling exponents  $\beta$  and  $\nu$  all change significantly from the quasi-steady-state to steady-state solutions because of the change in flow structure (Figs 1d and e), the scaling exponent  $n$  remains to satisfy eq. (6).

While these steady-state cases demonstrate that the flow structure and  $N_p$  may not change with  $Ra$  but may be sensitive to initial conditions or size of the model box, it is important to examine plume dynamics from high- $Ra$  models with intrinsically time-dependent solutions. Cases 11–14 are computed at  $Ra$  ranging from  $3 \times 10^6$  to  $10^8$  in a  $2 \times 2 \times 1$  box with random perturbations in the initial condition (Table 1). For this set of calculations we did not consider smaller  $Ra$  because models with smaller  $Ra$  are more dependent on initial

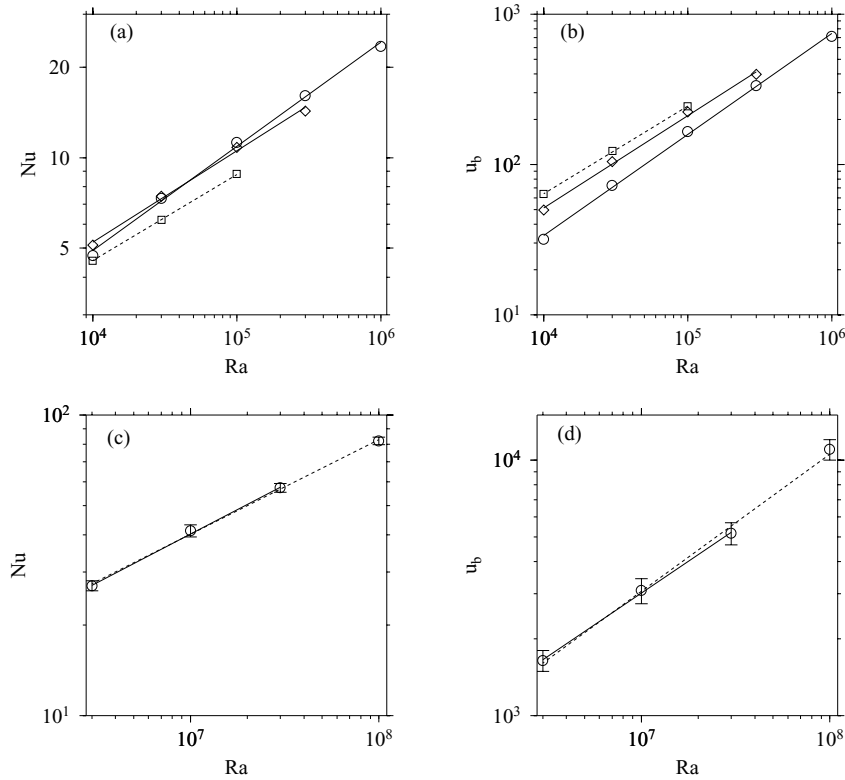


**Figure 3.** Dependence of  $Nu$  and  $u_b$  on  $Ra$ . For cases 1–5 (circles with thin solid line), the quasi-steady state of cases 7–10 (diamonds with thick solid line) and the steady state of cases 7–9 (squares with thin dashed line),  $Nu$  versus  $Ra$  (a) and  $u_b$  versus  $Ra$  (b). For cases 11–14,  $Nu$  versus  $Ra$  (c) and  $u_b$  versus  $Ra$  (d), both with standard deviations. In (a)–(d) the lines are the fittings to power-law functions. In (c) and (d) the solid and dashed lines represent the fittings for cases 11–13 and cases 11–14, respectively.

**Table 2.** Coefficient  $p$  and exponent  $q$  for fitting a power-law function  $pRa^q$ .

	Cases 1–5	Cases 7–10 <sup>a</sup>	Cases 7–9 <sup>a</sup>	Cases 11–14	Cases 11–13
$Nu^b$	(0.201, 0.347)	(0.322, 0.303)	(0.326, 0.286)	(0.250, 0.315)	(0.210, 0.326)
$u_b$	(0.0683, 0.673)	(0.182, 0.613)	(0.298, 0.583)	(0.542, 0.536)	(0.985, 0.498)
$n^c$	0.04	-0.01	-0.02	0.188	0.308

<sup>a</sup>Cases 7–10 are for the quasi-steady-state solutions, while cases 7–9 are for the final steady state.

<sup>b</sup> $p$  and  $q$  are given as  $(p, q)$ .

<sup>c</sup> $n$  is the predicted exponent for plume number and is equal to  $4(q_{Nu} - q_u/2)$ , where  $q_{Nu}$  and  $q_u$  are exponents for  $Nu$  and  $u_b$ , respectively (they are also given as  $\beta$  and  $\nu$ ).

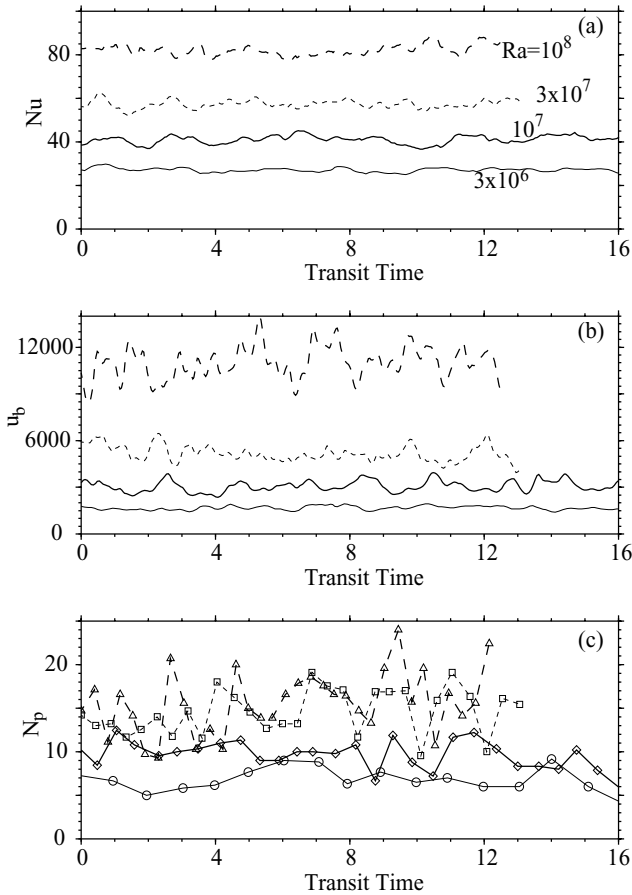


**Figure 4.** Time dependence of  $Nu$  (a),  $u_b$  (b) and  $N_p$  (c) for cases 11–14. Only the final 12–20 transit times of each case are shown. Each part uses the same line convention.  $N_p$  is measured every 500 time steps, and each symbol in (c) represents a measurement.

conditions and box size, as we have seen in previous cases. We chose a box with a moderate horizontal dimension to achieve a sufficiently high numerical resolution. For example, for case 14 with  $Ra = 10^8$ , we used  $320 \times 320 \times 96$  or nearly 10 million elements (Table 1), which just fit to one of our Beowulf clusters with 48 Gbyte RAM and 48 Xeon processors. At such a high  $Ra$ , the box size of  $2 \times 2 \times 1$  should not influence flow structure significantly. For all these cases, grid refinement is applied to the bottom and top boundary layers according to  $Ra$ . These cases are computed for at least 60 000 time steps and for more than 12 transit times after they reach a statistically steady state (see Figs 4a and b for time dependence of  $Nu$  and  $u_b$ ). The averaged properties of the flow and plumes are computed over at least 12 transit times after the solutions are in a statistically steady state.

If we group these four cases together and fit their time-averaged  $Nu$  and  $u_b$  to a power-law function of  $Ra$  we obtain  $Nu = 0.250Ra^{0.315}$  and  $u_b = 0.542Ra^{0.536}$  (Table 1 and Figs 3c and d with standard deviations). According to eq. (6), these exponents suggest that the exponent for  $N_p$ ,  $n$  is 0.188 (Table 2). That  $N_p$  increases with  $Ra$  is generally consistent with the flow structure for these cases (Fig. 5). The length scale of the flow becomes smaller and the number of upwelling and downwelling plumes increases, as  $Ra$  increases from  $3 \times 10^6$  to  $3 \times 10^7$  (Figs 5a, b and c). However, this trend does not seem to hold for case 14 with  $Ra = 10^8$  that displays a similar flow length scale to that of case 13 with  $Ra = 3 \times 10^7$  (Figs 5c and d). Using the algorithm outlined in Section 2.2 with  $f = 0.2$  and  $P_f = 5$  per cent, we determined the time dependence of  $N_p$  and  $N_{up}$  for each of these cases (Fig. 4c for  $N_p$ ). Time averages of  $N_p$ ,  $\langle N_p \rangle$ , for cases with  $Ra = 3 \times 10^6$ ,  $10^7$ ,  $3 \times 10^7$  and  $10^8$  are 7.1, 9.5, 14.6 and 15.5 respectively. The corresponding number of upwelling plumes  $\langle N_{up} \rangle$  is 3.7, 5.1, 8.2 and 7.0, for  $Ra = 3 \times 10^6$ ,  $10^7$ ,  $3 \times 10^7$  and  $10^8$ , respectively (Table 3 for  $\langle N_p \rangle$ ,  $\langle N_{up} \rangle$ , and their standard deviations). There is a significant time fluctuation in the number of plumes (e.g. Fig. 4c), as indicated by the standard deviations. However, it is clear that  $\langle N_p \rangle$  and  $\langle N_{up} \rangle$  in general increase with  $Ra$  (Figs 6a and b), consistent with the thermal structure (Fig. 5). It is also clear that  $\langle N_p \rangle$  and  $\langle N_{up} \rangle$  for case 14 with  $Ra = 10^8$  do not differ significantly from those for case 13 with  $Ra = 3 \times 10^7$ .

That  $\langle N_p \rangle$  appears to be saturated at  $Ra = 3 \times 10^7$  suggests that perhaps we should consider these cases differently. If we group cases 11–13 together, we find that  $Nu = 0.210Ra^{0.326}$  and  $u_b = 0.985Ra^{0.498}$ , which leads to the exponent for  $N_p$ ,  $n = 0.308$  from eq. (6) (Table 2). We can also fit  $\langle N_p \rangle$  for cases 11–13 to a power-law function of  $Ra$  as  $\langle N_p \rangle = 0.0678Ra^{0.310}$  (Table 3 and Fig. 6a). For the upwelling plumes, the power-law function is  $\langle N_{up} \rangle = 0.0222Ra^{0.342}$  (Table 3 and Fig. 6a). These exponents for plume scalings are similar to  $n = 0.308$  derived from eq. (6) with exponents  $\beta$  and  $\nu$  for  $Nu$  and  $u_b$ . It is also interesting to notice that if only cases 13 and 14 (i.e.  $Ra = 3 \times 10^7$  and  $10^8$ ) are considered, we obtain  $Nu = 0.335Ra^{0.299}$  and  $u_b = 0.103Ra^{0.629}$ , which leads to  $n = -0.06$  from eq. (6). This is consistent with the modelling results that  $N_p$  does not increase with  $Ra$  over this range of  $Ra$ . This further demonstrates that the simple analysis of boundary layer instabilities presented in Section 2.3 correctly describes the physics in these rather complicated numerical models.

We now examine the effects of parameters  $f$  and  $P_f$ . If  $f$  is reduced from 0.2 to 0.1,  $\langle N_p \rangle$  determined from our algorithm for each of cases 11–14 is reduced by  $\sim 1$ , and  $\langle N_{up} \rangle$  is reduced by  $\sim 0.5$  (Table 3). This  $\sim 10$  per cent reduction in number of plumes arises because a smaller  $f$  leads to smaller threshold temperature that defines plumes and hence a larger cross-sectional area for plumes, which with our algorithm causes some plumes to connect and become one plume. For cases 11–13, we found  $\langle N_p \rangle = 0.0622Ra^{0.309}$  and  $\langle N_{up} \rangle = 0.0237Ra^{0.332}$ , which have similar exponents to those

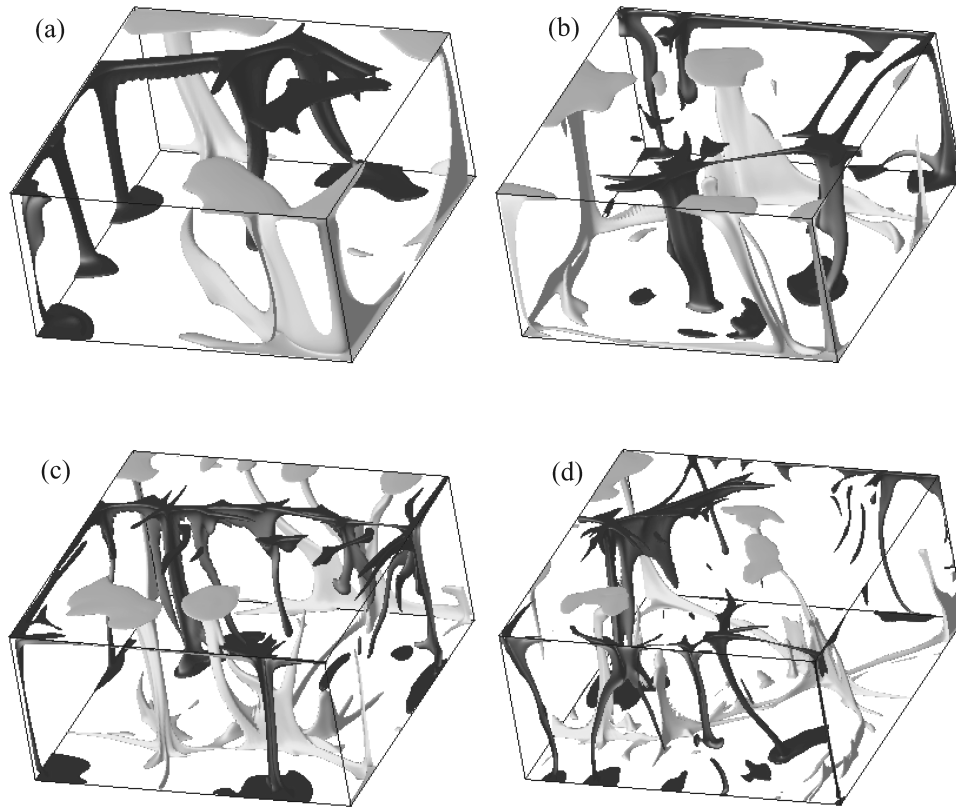


**Figure 5.** Representative 3-D thermal structure for cases 11 (a), 12 (b), 13 (c) and 14 (d). The figure shows isosurfaces of residual temperature  $\delta T = T - T_{ave}(z)$  with  $\delta T = 0.2$  (light shading) and  $-0.2$  (dark shading), respectively.

**Table 3.** The number, area, and vertical velocity of plumes for cases 11–14.

	$f$	$P_f$	Case 11 <sup>a</sup>	Case 12	Case 13	Case 14	$(p, q)^b$
$\langle N_{up} \rangle$	0.4	0.05	3.95(1.27)	5.59(1.53)	8.16(2.00)	6.26(1.90)	(0.0358, 0.315)
	0.2	0.05	3.74(1.11)	5.15(1.42)	8.23(1.90)	7.00(1.95)	(0.0222, 0.342)
	0.1	0.05	3.48(1.04)	4.61(1.24)	7.51(1.83)	6.63(2.12)	(0.0237, 0.332)
$\langle N_p \rangle$	0.4	0.05	7.85(1.44)	10.5(1.93)	14.3(3.03)	14.3(3.09)	(0.164, 0.259)
	0.2	0.05	7.13(1.49)	9.49(1.80)	14.6(2.61)	15.5(3.55)	(0.0678, 0.310)
	0.1	0.05	6.44(1.41)	8.60(1.75)	13.2(2.25)	15.1(3.36)	(0.0622, 0.309)
$\langle N_{up} \rangle$	0.4	0.10	3.32(1.55)	4.76(1.52)	6.71(1.65)	4.96(1.84)	(0.0345, 0.306)
	0.2	0.10	2.90(0.99)	4.34(1.41)	6.85(1.74)	5.35(1.84)	(0.0109, 0.373)
	0.1	0.10	2.82(0.95)	3.80(1.19)	6.08(2.01)	4.99(1.88)	(0.0191, 0.333)
$\langle N_p \rangle$	0.4	0.10	6.89(1.50)	9.21(1.93)	11.8(2.53)	10.8(2.74)	(0.217, 0.232)
	0.2	0.10	5.97(1.42)	8.06(1.90)	12.3(2.51)	11.6(3.39)	(0.0565, 0.311)
	0.1	0.10	5.52(1.37)	7.08(1.76)	11.0(2.34)	11.1(3.22)	(0.0637, 0.297)
$\langle A_{up} \rangle (\times 10^{-3})$	0.4	0.05	6.87(1.71)	3.96(1.61)	1.89(0.48)	1.35(0.38)	(29.5, -0.558)
	0.2	0.05	24.8(20.5)	10.8(4.59)	5.08(1.23)	3.76(1.18)	(728, -0.690)
	0.1	0.05	45.2(32.8)	20.1(9.39)	9.44(2.25)	7.65(2.62)	(1150, -0.680)
$\langle V_{up} \rangle (\times 10^3)$	0.4	0.05	3.59(0.52)	7.58(1.13)	13.3(1.51)	30.2(4.38)	(0.737, 0.571)
	0.2	0.05	3.04(0.42)	6.88(1.19)	12.3(1.27)	26.2(3.44)	(0.368, 0.606)
	0.1	0.05	2.85(0.41)	6.35(0.99)	11.7(1.40)	24.5(3.41)	(0.314, 0.613)

<sup>a</sup>The numbers in the round brackets under each case column are the standard deviation.

<sup>b</sup> $p$  and  $q$  are the coefficient and exponent of a power-law function  $pRa^q$  for cases 11–13.

with  $f = 0.2$  (Table 3 and Figs 6a and b). Not surprisingly, if  $f$  is increased from 0.2 to 0.4, the number of plumes for each case on average increases by  $\sim 10$  per cent. For  $f = 0.4$ , we found  $\langle N_p \rangle = 0.164Ra^{0.259}$  and  $\langle N_{up} \rangle = 0.0358Ra^{0.315}$  for cases 11–13, which are again similar to those with  $f = 0.2$  (Table 3 and Figs 6a and b). The exponents for  $\langle N_p \rangle$  and  $\langle N_{up} \rangle$  averaged for  $f = 0.1, 0.2$  and  $0.4$  are 0.293 and 0.330, respectively.

If we increase  $P_f$  from 5 per cent to 10 per cent (i.e. only plumes that carry heat flux that is greater than 10 per cent of the strongest plume are counted), the number of plumes is reduced by 20 per cent for all cases (Table 3). For  $f = 0.2$  we found  $\langle N_p \rangle = 0.0565Ra^{0.311}$  and  $\langle N_{up} \rangle = 0.0109Ra^{0.373}$  for cases 11–13. For  $P_f = 10$  per cent, the exponents for  $\langle N_p \rangle$  and  $\langle N_{up} \rangle$  averaged for  $f = 0.1, 0.2$  and  $0.4$  are 0.280 and 0.337, respectively. These scaling exponents for

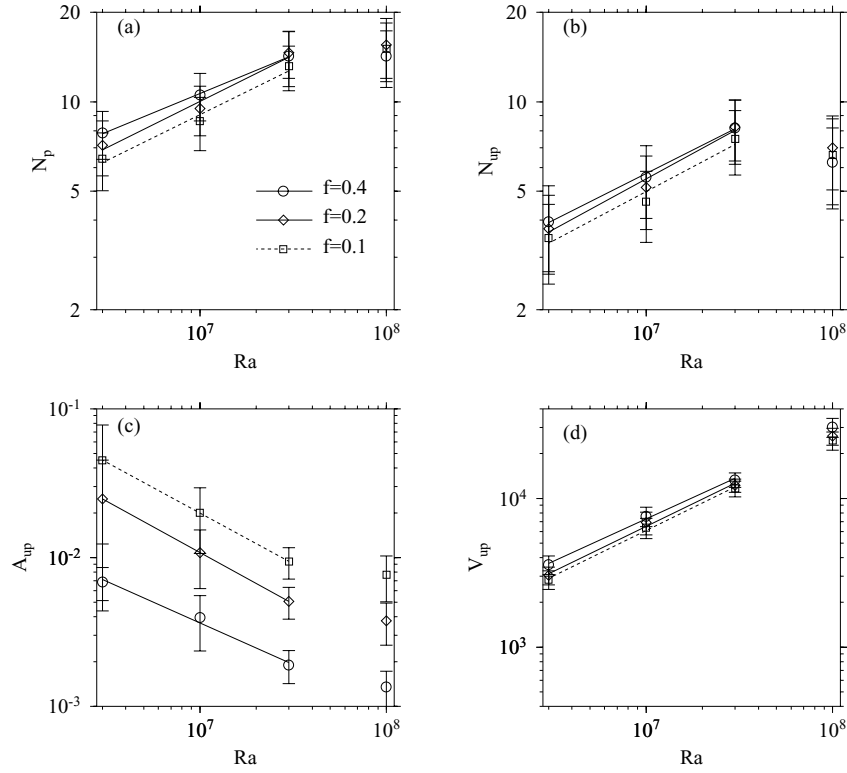


**Figure 6.** Dependence of  $N_p$  (a),  $N_{up}$  (b),  $A_{up}$  (c) and  $V_{up}$  (d) on  $Ra$  for cases 11–14. Circles, diamonds and squares are for  $f = 0.4, 0.2$  and  $0.1$ , respectively. The lines are the fittings to power-law functions for cases 11–13.

plume number are similar to  $n = 0.308$  derived from exponents  $\beta$  and  $\nu$  based on eq. (6). If we include all the plumes by decreasing  $P_f$  from 5 per cent to 0.1 per cent, the number of plumes on average increases by  $\sim 35$  per cent for all the cases. Further decrease in  $P_f$  has almost no effect on the number of plumes. This suggests that there cannot be a large number of small plumes present in these models.

In summary, we found that the effects of  $Ra$  on plume number depend on the range of  $Ra$ . For  $Ra < 10^6$ , plume number may not be sensitive to  $Ra$ . For  $Ra$  varying from  $3 \times 10^6$  to  $3 \times 10^7$  (i.e. cases 11–13),  $\langle N_p \rangle$  and  $\langle N_{up} \rangle$  scale with  $Ra$  to the power of  $n \sim 0.31$  (i.e. cases 11–13), as determined either directly from fitting the number of plumes for these cases or from our boundary layer instability analysis (i.e. eq. 6) in combination with scalings for global quantities  $Nu$  and  $u_b$ . This implies that plume spacing  $\lambda \sim Ra^{-n/2}$

$\sim Ra^{-0.16}$  in this  $Ra$  range. However, this scaling may not hold for larger  $Ra$  and plume number does not change significantly from  $Ra = 3 \times 10^7$  to  $Ra = 10^8$ .

### 3.2 Size, vertical velocity and heat transfer of upwelling plumes

For all these cases, we also quantified the averaged cross-sectional area per plume  $A_{up}$ , averaged vertical velocity  $V_{up}$  and plume heat flux for upwelling plumes in the depth range of  $0.45 \leq z \leq 0.55$ . For the steady-state cases with  $Ra$  varying from  $10^4$  to  $10^6$  (cases 1–5), there are two upwelling and two downwelling plumes all having the same plume heat flux, and  $A_{up}$  decreases with  $Ra$  and  $f$  (Table 4 and Fig. 7a). A larger  $f$  leads to a larger threshold temperature that defines upwelling plumes and hence a smaller cross-sectional

**Table 4.** The area and vertical velocity of upwelling plumes for cases 1–5.

	$f$	Case 1	Case 2	Case 3	Case 4	Case 5	$(p, q)^a$
$A_{up} (\times 10^{-2})$	0.4	5.40	2.73	1.55	0.868	0.513	(5.47, $-0.508$ )
	0.2	9.61	5.07	2.64	1.69	0.952	(8.77, $-0.497$ )
	0.1	13.9	7.39	4.06	2.38	1.40	(12.8, $-0.497$ )
$V_{up}$	0.4	67.4	176.9	458.2	1030.6	2452	(0.0561, 0.777)
	0.2	56.5	154.5	416.6	942.6	2286	(0.0388, 0.800)
	0.1	47.6	135.8	370.4	870.4	2120	(0.0272, 0.821)
$R_{up}^b$	—	0.240	0.175	0.130	0.101	0.0749	(2.35, $-0.250$ )
$A_{up} (\times 10^{-2})$	—	4.51	2.34	1.30	0.825	0.449	(3.93, $-0.491$ )
	—	70.0	181.8	470.2	1059	2544	(0.0579, 0.777)

<sup>a</sup>  $p$  and  $q$  are the coefficient and exponent of a power-law function  $pRa^q$  for cases 1–5.

<sup>b</sup>  $R_{up}$  is from fitting temperature to an exponential function in eq. (5).  $A_{up}$  and  $V_{up}$  below the line for this radius are the area and average vertical velocity of plumes defined by this radius. Also notice that the plumes are not perfectly cylindrical.

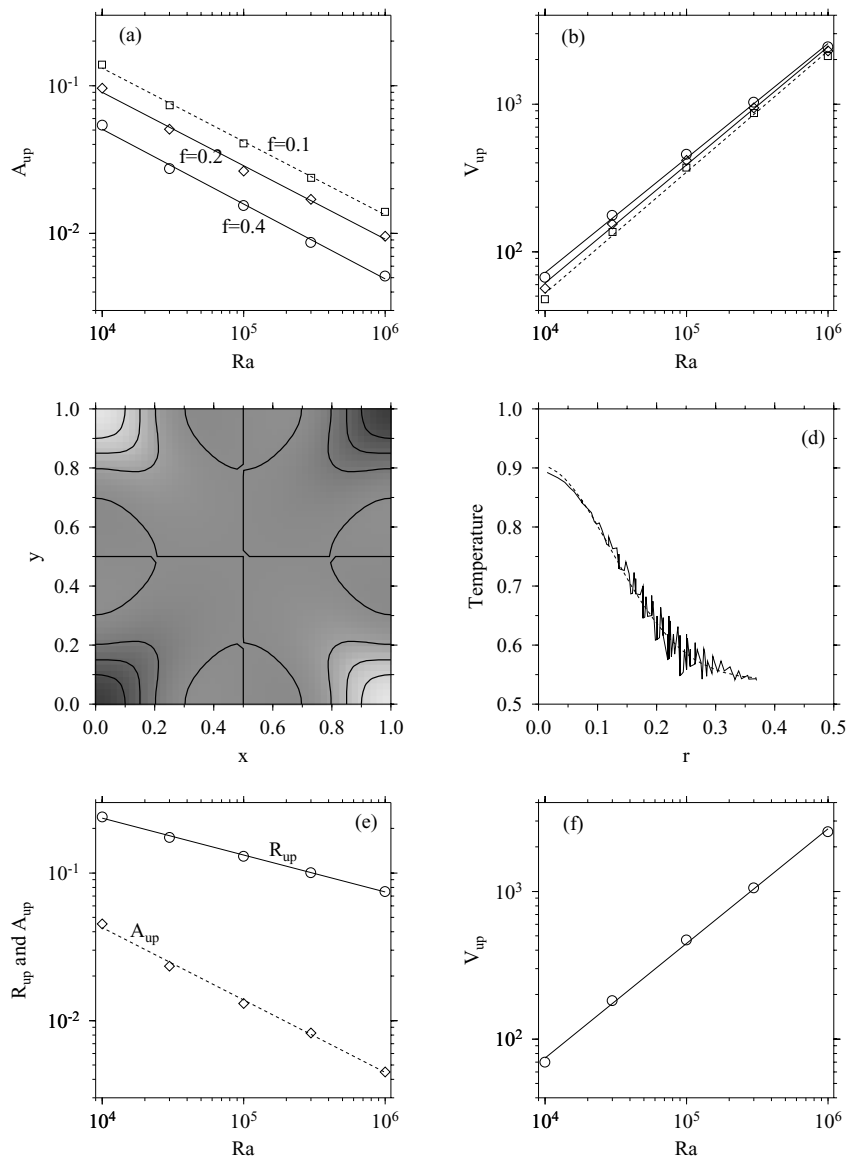


**Figure 7.** Dependence of  $A_{\text{up}}$  (a) and  $V_{\text{up}}$  (b) on  $Ra$  for cases 1–5; for case 2, the temperature structure at  $z = 0.5$  (c) and the temperature at  $z = 0.5$  as a function of distance from the centre of the upwelling plume (solid line) and its fitting to an exponential function (dashed line) (d); and  $Ra$ -dependence of  $R_{\text{up}}$  and  $A_{\text{up}}$  (e) and  $V_{\text{up}}$  (f) for cases 1–5 that are determined by fitting to an exponential function.

area for the plumes. The power-law fittings are  $A_{\text{up}} = 12.79Ra^{-0.497}$ ,  $A_{\text{up}} = 8.77Ra^{-0.497}$  and  $A_{\text{up}} = 5.47Ra^{-0.508}$ , for  $f = 0.1, 0.2$  and  $0.4$ , respectively (Table 4 and Fig. 7a). Notice that the power-law exponents for  $A_{\text{up}}$  are all close to  $-0.5$  (the averaged exponent is  $-0.50$ ). This also implies that averaged plume radius  $R_{\text{up}} \sim Ra^{-0.25}$ . The averaged vertical velocity for upwelling plumes increases with  $Ra$  and scales as  $V_{\text{up}} = 0.0272Ra^{0.821}$ ,  $V_{\text{up}} = 0.0388Ra^{0.800}$  and  $V_{\text{up}} = 0.0561Ra^{0.777}$ , for  $f = 0.1, 0.2$  and  $0.4$ , respectively (Table 4 and Fig. 7b). The averaged exponent for  $V_{\text{up}}$  for different  $f$  is  $0.799$ . On average, the upwelling plumes for these cases transfer heat fluxes that are 48 per cent, 44 per cent and 35 per cent of the total surface heat flux, for  $f = 0.1, 0.2$  and  $0.4$ , respectively. The smaller percentage for larger  $f$  arises because a larger  $f$  leads to a smaller plume area. However, for a given  $f$ , the percentage of plume heat flux to the total surface or bottom heat flux is nearly the same for different  $Ra$ .

For each of cases 1–5, we also determined  $R_{\text{up}}$  by fitting to eq. (5) the temperature of an upwelling plume as a function of distance to the plume centre in the depth range of  $0.45 \leq z \leq 0.55$ . We then used  $R_{\text{up}}$  to determine  $A_{\text{up}}$  and  $V_{\text{up}}$ . With this approach, we do not need parameter  $f$  to characterize plumes. An example is given in Figs 7c and d for case 2 at  $z = 0.5$ . For this case,  $R_{\text{up}}$  is determined to be  $0.175$  and  $A_{\text{up}}$  and  $V_{\text{up}}$  are determined as  $0.0234$  and  $181.8$ , respectively (Table 4). Notice that  $A_{\text{up}}$  is not exactly equal to  $\pi R_{\text{up}}^2/4$  because the plumes are not perfectly cylindrical (Fig. 7c). In fact, this imperfect cylindrical geometry for plumes causes the fluctuation in temperature in Fig. 7d (note that this temperature is a collection of temperatures at gridpoints near the plume). With this approach, we found that  $R_{\text{up}} = 2.35Ra^{-0.250}$ ,  $A_{\text{up}} = 3.93Ra^{-0.491}$  and  $V_{\text{up}} = 0.0579Ra^{0.777}$  (Table 4 and Figs 7e and f), and these scaling exponents compare well with those determined from the other approach with parameter  $f$ .

These scaling relationships for plume area and velocity can also be compared with the scaling analyses in Section 2.3. For cases 1–5  $n = 0$  and  $\beta = 0.347$ , and using eqs (11) and (12) we have  $R_{\text{up}} \sim Ra^{-0.22}$ ,  $A_{\text{up}} \sim Ra^{-0.435}$  and  $V_{\text{up}} \sim Ra^{0.782}$ . If we use  $\beta = 1/3$ ,  $R_{\text{up}} \sim Ra^{-2/9} = Ra^{-0.222}$ ,  $A_{\text{up}} \sim Ra^{-4/9} = Ra^{-0.444}$  and  $V_{\text{up}} \sim Ra^{7/9} = Ra^{0.777}$ . These scaling exponents compare reasonably well with our numerical results.

For time-dependent cases in which the number of plumes increases with  $Ra$  (i.e. cases 11–13), for  $f = 0.2$  and  $P_f = 0.05$  we found  $A_{\text{up}} = 728.3Ra^{-0.690}$  and  $V_{\text{up}} = 0.369Ra^{0.606}$  (Table 3 and Figs 6c and d). When being averaged over  $f = 0.1, 0.2$  and  $0.4$ , the exponents for  $A_{\text{up}}$  and  $V_{\text{up}}$  are  $-0.643$  and  $0.597$ , respectively. For these cases,  $\beta = 0.326$  and  $n = 0.308$  as determined from  $Nu$  and  $u_b$  (Table 2), and substituting them into eqs (11) and (12) leads to  $R_{\text{up}} \sim Ra^{-0.276}$ ,  $A_{\text{up}} \sim Ra^{-0.552}$  and  $V_{\text{up}} \sim Ra^{0.570}$ . These scaling exponents compare reasonably well with averaged exponents for  $A_{\text{up}}$  and  $V_{\text{up}}$ :  $-0.643$  and  $0.597$ . The difference may be partly caused by the relatively large variations in plume strength among the plumes that we average. With  $P_f = 0.05$ , heat flux carried by upwelling plumes on average accounts for 22.9, 39 and 47 per cent of the total surface heat flux, for  $f = 0.4, 0.2$  and  $0.1$ , respectively. With  $P_f = 0.001$ , these percentages increase slightly to 23.2, 40 and 48.2 per cent, for  $f = 0.4, 0.2$  and  $0.1$  respectively. This indicates that although when  $P_f$  is reduced from 0.05 to 0.001 the count of plumes may increase by  $\sim 30$  per cent, the plume heat flux from these weak plumes is rather insignificant.

#### 4 DISCUSSION

An important question that we want to address in this paper is how plume number and plume spacing depend on the vigour of convection or  $Ra$ . Our results for isoviscous and basal heating thermal convection indicate that plume number may not have a monotonic dependence on  $Ra$ . At relatively small  $Ra$ , as  $Ra$  increases, the increased plume velocity is sufficient to compensate for the effects of decreased plume area and to maintain the increased heat flux with  $Ra$  (heat flux or  $Nu \sim Ra^{1/3}$ ) with no change in plume number. At moderately large  $Ra$  ( $3 \times 10^6$  to  $3 \times 10^7$ ) our results indicate that plume number scales as  $Ra^{0.31}$  and that plume spacing  $\lambda \sim Ra^{-0.16} \sim \delta^{1/2}$  (note that  $\delta \sim Ra^{-1/3}$  for our models). However, at relatively large  $Ra$  ( $\sim 10^8$ ), plume number does not increase with  $Ra$ .

This result on plume number scaling is different from previous studies that suggested a monotonic increase of plume number with  $Ra$  (e.g. Solomatov 2004; Parmentier & Sotin 2000). Using a scaling

analysis and 3-D numerical simulations, Parmentier & Sotin (2000) suggested that for an entirely internal heating convection the number of downwelling plumes scales with  $Ra^{1/4}$  and the plume scaling  $\lambda \sim Ra^{-1/8} \sim \delta^{1/2}$  for  $Ra$  varying from  $3 \times 10^6$  to  $3 \times 10^9$  (note  $\delta \sim Ra^{-1/4}$  for internal heating convection). Although we also found that  $\lambda \sim \delta^{1/2}$ , it only holds for  $Ra$  between  $3 \times 10^6$  and  $3 \times 10^7$ . The difference between our results and those of Parmentier & Sotin (2000) may result from the difference in our convection models (i.e. basal heating versus internal heating). Another difference is that we counted plumes at the mid-depth of the box while Parmentier & Sotin (2000) counted plumes right below the TBL. Weak plumes may dissipate away or merge together to form stronger ones as they descend (ascend) after they are derived from the top (bottom) TBL (Vincent & Yuen 1988; Parmentier & Sotin 2000; Labrosse 2002). This effect can be best seen in 2-D thermal convection with a high  $Ra$  (see Fig. 8 for a basal heating and isoviscous calculation with  $Ra = 10^8$  with more details in the figure caption). This snapshot of temperature and flow field is representative of the statistically steady state for this case. Although plumes (or sheets) develop frequently from both the top and bottom TBLs, most of them merge into three plumes (one upwelling and two downwelling plumes) that are capable of passing through the mid-depth of the box (Fig. 8). The large-scale flow structure is controlled by these three plumes, and the other weak plumes only have secondary effects (Fig. 8).

In this study, because we are interested in the number of upwelling plumes that may reach the surface, it is more appropriate for us to count the plumes at the mid-depth of the box. Because our plumes are directly related to global flow field and heat transfer, this enables us to compare plume number from our numerical models with the prediction from our scaling analyses that are based on global physical quantities including  $Nu$  and  $u_b$  (i.e. eq. 6:  $n = 4\beta - 2v$ , where  $n$ ,  $\beta$  and  $v$  are the scaling exponents for plume number,  $Nu$  and  $u_b$ , respectively). In particular, our analyses suggest that if  $v = 2\beta$ , then plume number is independent of  $Ra$  (i.e.  $n = 0$ ). For  $n > 0$  or when plume number increases with  $Ra$ ,  $v$  must be smaller than  $2\beta$ . Our results also show that  $n$  has significant effects on how the vertical velocity and cross-sectional area of plumes scale with  $Ra$  (eqs 11 and 12).

That the plume spacing  $\lambda$  has a lower bound (or plume number has an upper bound) as  $Ra$  increases suggests that the box depth is an important length scale that limits the plume spacing and number. Although this was suggested by Davies (1998), our numerical experiments provide direct support for it. A simple physical argument may be made on the basis of viscous dissipation: when  $\lambda$  gets much smaller than the box depth, this would lead to too great a viscous

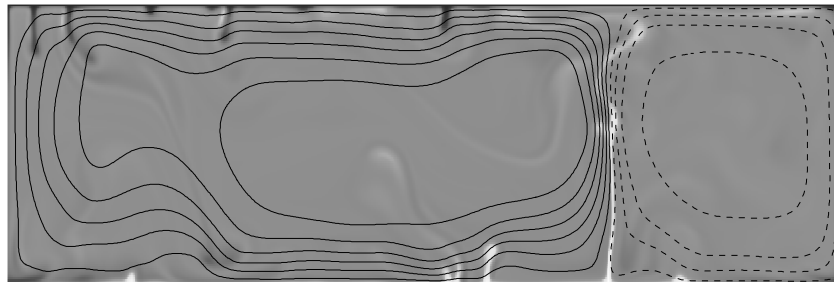


**Figure 8.** Temperature and flow fields (stream function) for a 2-D isoviscous and basal heating convection calculation at  $Ra = 10^8$  in a box with an aspect ratio of 3 and the same boundary and initial conditions as in the 3-D case 14. For this calculation, 128 and 576 elements are used in vertical and horizontal directions, respectively, and grid refinement is applied to the bottom and top boundaries. Negative stream functions (dashed lines) are for clockwise circulation, while positive stream functions (solid lines) are for counter-clockwise circulation.

dissipation, i.e. inefficient heat transfer. This result on the scaling of plume spacing has implications for studies of plume dynamics.

If plume number does not increase indefinitely with  $Ra$ , as our results suggest, then we should probably not expect thousands of upwelling plumes in the mantle that display a power-law relationship between plume number and the plume heat flux, as suggested by Malamud & Turcotte (1999). This also suggests that the plume heat flux constrained by the hotspot swell topography and gravity anomalies (Davies 1988; Sleep 1990) may reflect the true heat flux carried by mantle plumes. However, to what extent this plume heat flux represents the heat flux from the core or the bottom layer of a layered mantle is an open question. Our models for basal heating and isoviscous convection show that the heat flux from upwelling plumes only accounts for 50 per cent of the bottom heat flux, independent of  $Ra$ . This is consistent with the work of Labrosse (2002) who examined the plume heat flux for isoviscous thermal convection with a mixed heating mode.

There are a number of aspects of this study that need more work. First, it would be useful to perform more calculations with  $Ra$  higher than  $10^8$  to further examine the dependence of plume number on  $Ra$ . Second, we should consider the effects of temperature-dependent viscosity and internal heating. These calculations are rather expensive at the moment, as they need even higher resolutions and encompass more parameters (e.g. internal heating rate and activation energy). However, with the rapid improvement in computational power, these calculations will become feasible in the near future. Third, although it is found that thermal convection with surface mobile plates often displays similar heat transfer characteristics to isoviscous thermal convection (Gurnis 1989) it is unclear to what extent our results on plume dynamics from isoviscous thermal convection are influenced by surface plates (Jellinek *et al.* 2003; Gonnermann *et al.* 2004). It is important to examine such effects in future work.

## 5 CONCLUSIONS

With numerical modelling and scaling analyses we investigated the effects of  $Ra$  on the dynamics of thermal plumes including plume number, plume spacing, plume vertical velocity and plume radius in 3-D isoviscous and basal heating thermal convection. Our results can be summarized as follows:

(1) The scaling exponents for plume number,  $n$ , heat flux or  $Nu$ ,  $\beta$  and average horizontal velocity on the bottom boundary,  $v$ , satisfy  $n = 4\beta - 2v$ .

(2) At relatively small  $Ra$  ( $\leq 10^6$ ), plume number is insensitive to  $Ra$ . For  $3 \times 10^6 \leq Ra \leq 3 \times 10^7$  it is found that plume number scales as  $Ra^{0.31}$  and plume spacing  $\lambda$  scales as  $Ra^{-0.16}$  or  $\delta^{1/2}$ , where  $\delta$  is the boundary layer thickness. However, for larger  $Ra$  ( $\sim 10^8$ ) plume number and plume spacing become insensitive to  $Ra$  again. This indicates that plume number does not increase with  $Ra$  monotonically and that the box depth poses an important limit on plume spacing at very large  $Ra$ .

(3) Our scaling analyses indicate that vertical velocity in upwelling plumes  $V_{up} \sim Ra^{2(1-n+\beta/2)/3}$  and that plume radius  $R_{up} \sim Ra^{(\beta-1-n/2)/3}$ .

(4) For relatively small  $Ra$  ( $\leq 10^6$ ), with  $n = 0$  and  $\beta = 1/3$ , the scaling analyses lead to  $V_{up} \sim Ra^{7/9} \sim Ra^{0.778}$  and  $R_{up} \sim Ra^{-2/9} \sim Ra^{-0.222}$ , both of which differ from the scalings for the bottom boundary velocity and boundary layer thickness. These scaling relationships can be compared with those from numerical models:  $V_{up} \sim Ra^{0.777}$  and  $R_{up} \sim Ra^{-0.250}$ .

(5) For  $3 \times 10^6 \leq Ra \leq 3 \times 10^7$ , with  $\beta = 0.326$  and  $n = 0.31$ , the scaling analysis leads to  $V_{up} \sim Ra^{0.570}$  and  $R_{up} \sim Ra^{-0.276}$ , in comparison with the scaling from numerical models:  $V_{up} \sim Ra^{0.597}$  and  $R_{up} \sim Ra^{-0.322}$ .

## ACKNOWLEDGMENTS

The author thanks E. M. Parmentier for helpful discussions and Norm Sleep and an anonymous reviewer for comments. This research is supported by NSF under grant number EAR-0134939 and the David and Lucile Packard Foundation.

## REFERENCES

- Burke, K.C. & Wilson, J.T., 1976. Hotspots on the earth's surface, *Sci. Am.*, **235**, 46–57.
- Courtilot, V., Davaille, A., Besse, J. & Stock, J., 2003. Three distinct types of hotspots in the Earth's mantle, *Earth planet. Sci. Lett.*, **205**, 295–308.
- Crough, T.S., 1983. Hotspot swells, *Annu. Rev. Earth Planet. Sci.*, **11**, 165–193.
- Davies, G.F., 1988. Ocean bathymetry and mantle convection, 1. Large-scale flow and hotspots, *J. geophys. Res.*, **93**, 10 467–10 489.
- Davies, G.F., 1998. Topography: a robust constraint on mantle fluxes, *Chem. Geol.*, **145**, 479–489.
- Gonnermann, H.M., Jellinek, A.M., Richards, M.A. & Manga, M., 2004. Modulation of mantle plumes and heat flow at the core mantle boundary by plate-scale flow: results from laboratory experiments, *Earth planet. Sci. Lett.*, **226**, 53–67.
- Gurnis, M., 1989. A reassessment of the heat transport by variable viscosity convection with plates and lids, *Geophys. Res. Lett.*, **16**, 179–182.
- Howard, L.N., 1966. Convection at high Rayleigh number, in *Proceedings of the 11th International Congress on Applied Mechanics*, pp. 1109–1115, ed. Gortler, H., Springer, Berlin.
- Jellinek, A.M., Gonnermann, H.M. & Richards, M.A., 2003. Plume capture by divergent plate motions: implications for the distribution of hotspots, geochemistry of mid-ocean ridge basalts, and estimates of the heat flux at the core–mantle boundary, *Earth planet. Sci. Lett.*, **205**, 361–378.
- Labrosse, S., 2002. Hotspots, mantle plumes and core heat loss, *Earth planet. Sci. Lett.*, **199**, 147–156.
- Malamud, B.D. & Turcotte, D.L., 1999. How many plumes are there?, *Earth planet. Sci. Lett.*, **174**, 113–124.
- Malevsky, V. & Yuen, D.A., 1993. Plume structures in the hard-turbulent regime of three-dimensional infinite Prandtl number convection, *Geophys. Res. Lett.*, **20**, 383–386.
- McKenzie, D.P., Roberts, J.M. & Weiss, N.O., 1974. Convection in the Earth's mantle: Towards a numerical simulation, *J. Fluid Mech.*, **62**, 465–538.
- Montelli, R., Nolet, G., Dahlen, F.A., Masters, G., Engdahl, E.R. & Hung, S.H., 2004. Finite frequency tomography reveals a variety of plumes in the mantle, *Science*, **303**, 338–343.
- Moresi, L.N. & Solomatov, V.S., 1995. Numerical investigation of 2D convection with extremely large viscosity variation, *Phys. Fluids*, **9**, 2154–2164.
- Morgan, W.J., 1963. Convection plumes in the lower mantle, *Nature*, **230**, 43–43.
- Morgan, W.J., 1981. Hotspot tracks and the opening of the Atlantic and Indian Oceans, in *The Sea*, pp. 443–487, ed. Emiliani, C., Wiley, New York.
- Olson, P., 1990. Hotspots, swells, and mantle plumes, in *Magma Transport and Storage*, pp. 33–51, ed. Ryan, M.P., John Wiley, Chichester.
- Parmentier, E.M. & Sotin, C., 2000. Three-dimensional numerical experiments on thermal convection in a very viscous fluid: Implications for the dynamics of a thermal boundary layer at high Rayleigh number, *Phys. Fluids*, **12**, 609–617.

- Parmentier, E.M., Sotin, C. & Travis, B.J., 1994. Turbulent 3-D thermal convection in an infinite Prandtl number, volumetrically heated fluid: implications for mantle dynamics, *Geophys. J. Int.*, **116**, 241–251.
- Ribe, N.M. & Devalpine, D.P., 1994. The global hotspot distribution and instability of D, *Geophys. Res. Lett.*, **21**, 1507–1510.
- Richards, M.A., Duncan, R.A. & Courtillot, V.E., 1989. Flood basalts and hot-spot tracks: plume heads and tails, *Science*, **246**, 103–107.
- Romanowicz, B. & Gung, Y.C., 2002. Superplumes from the core-mantle boundary to the lithosphere: implications for heat flux, *Science*, **296**, 513–516.
- Schaeffer, N. & Manga, M., 2001. Interactions between rising and sinking mantle plumes, *Geophys. Res. Lett.*, **28**, 455–458.
- Sleep, N.H., 1987. Lithospheric heating by mantle plumes, *Geophys. J. R. astr. Soc.*, **91**, 1–12.
- Sleep, N.H., 1990. Hotspots and mantle plumes: some phenomenology, *J. geophys. Res.*, **95**, 6715–6736.
- Solomatov, V.S., 2004. Initiation of subduction by scale-scale convection, *J. geophys. Res.*, **109**, B01412, doi:10.1029/2003JB002628.
- Turcotte, D.L. & Schubert, G., 2002. *Geodynamics*, 2nd edn., Cambridge University Press, Cambridge.
- Vincent, A.P. & Yuen, D.A., 1988. Thermal attractor in chaotic convection with high-Prandtl-number fluids, *Phys. Rev. A*, **38**, 328–334.
- Weeraratne, D. & Manga, M., 1998. Transitions in the style of mantle convection at high Rayleigh numbers, *Earth planet. Sci. Lett.*, **160**, 563–568.
- Wilson, J.T., 1963. A possible origin of the Hawaiian islands, *Can. J. Phys.*, **41**, 863–870.
- Wolfe, C.J., Bjarnason, I.T., Vandecar, J.C. & Solomon, S.C., 1997. Seismic structure of the Iceland mantle plume, *Nature*, **385**, 245–247.
- Zhao, D.P., 2004. Global tomographic images of mantle plumes and subducting slabs: insight into deep Earth dynamics, *Phys. Earth planet. Int.*, **146**, 3–34.
- Zhong, S., Zuber, M.T., Moresi, L.N. & Gurnis, M., 2000. Role of temperature dependent viscosity and surface plates in spherical shell models of mantle convection, *J. geophys. Res.*, **105**, 11 063–11 082.